Two-dimensional high-bandwidth Shack-Hartmann wavefront sensor: design guidelines and evaluation testing

Shaddy Abado, MEMBER SPIE
Stanislav Gordeyev
Eric J. Jumper
University of Notre Dame
Center for Flow Physics and Control
Notre Dame, Indiana 46556
E-mail: sabado@nd.edu

Abstract. A novel two-dimensional high-bandwidth Shack-Hartmann wavefront sensor was designed and tested, addressing the high temporal bandwidth of aero-optical aberrations caused by compressible flows. The principle of operation and modifications from an earlier version of the wavefront sensor are presented and compared with a commercially available wavefront sensor with a 33×44 subaperture spatial resolution. A two-dimensional wavefront reconstruction algorithm is presented. The comparison was performed over a two-dimensional, acoustically forced heated jet. The high temporal resolution and spatial resolution of the sensor are demonstrated. The results show good agreement between the two sensors. © *2010 Society of Photo-Optical Instrumentation Engineers.*
[DOI: 10.1117/1.3454383]

1 Introduction

When a perfectly collimated, planar beam of light propagates through a field with variable index of refraction, it becomes distorted, resulting in significant reduction in the optical intensity in the far field, and degradation in overall performance of a light-transmitting system. When the transmitting system is airborne, and the variable-index-of-refraction turbulent flow is created by the aircraft, the effect is called the aero-optical problem.[1]

Contrary to atmospheric optical aberrations, which are caused by temperature gradients in the far field and characterized by low temporal frequencies[2] of less than a kilohertz, the aero-optically active aberration area is in the near field and caused by density variations due to boundary layers, separated shear layers, and wakes around an aircraft; these aberrations are characterized by high temporal frequencies,[3] typically around several kilohertz. In this context, the terms "near field" and "far field" do not refer to the Fresnel and Fraunhofer diffractions as defined by Fresnel number,[4] but to distortion regions with respect to the beam aperture size A; aero-optical effects are caused by a compressible turbulent flow around the airborne platform and characterized by a region on the order of several apertures, while atmospheric propagation effects are due to temperature fluctuations in the atmosphere, extending from just beyond the aircraft to the target. The fluctuations in the index of refraction n can be related to those in the density ρ by the Gladstone-Dale relation[5]

$$n = 1 + \rho K_{GD}, \tag{1}$$

where K_{GD} is the Gladstone-Dale constant.

To measure optical aberrations, compensate for the intensity losses, and maximize the propagated beam energy on a target, a closed-loop adaptive optics (AO) system is typically used.[6] It was shown by Nightingale et al.[3] that in order to develop an adaptive optics system that is capable of operating in a real flight scenario, a wavefront sensor (WFS) with a real-time framing rate that is on the order of 100 times of the bandwidth of an aberration is required. This requirement is in order to keep the feedback approach stable where only $\sim 1/10$ of the residual error can be removed for each deformable mirror (DM) update. In addition, a bandwidth requirement is set by the aberration flow field: In order to achieve a Strehl ratio[6] equal to 0.8, an aberration must be removed ten times per aberration-coherence-length clearing time.

As was mentioned, aero-optical disturbances are characterized by high temporal frequencies, around several kilohertz; hence a WFS that operates with a real-time sampling rate of hundreds of kilohertz is required. Current state-of-the-art conventional adaptive optics systems are limited to a bandwidth of hundreds of hertz for disturbance correction, making them unsuitable to compensate aero-optics-related intensity losses; different approaches need to be considered to compensate for the aero-optical aberration effects on the transmitted beam. In addition, the WFS should minimize the delay between sensing and calculating wavefronts, for the adaptive-optics system to be stable.[3] Such high framing rates and fast wavefront reconstruction are beyond the current capability of most commercially available, digital charge-coupled device (CCD) WFSs; there is a need to design a high-bandwidth WFS that does not use CCD technology.

Wavefront aberrations are commonly quantified using the optical path difference (OPD), which is the spatial-mean-removed optical path length (OPL). The OPL is de-
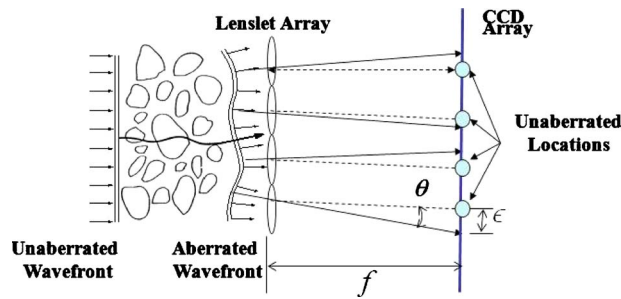
Fig. 1 Shack-Hartmann wavefront sensor: principle of operation.

fined as the path integral of the index-of-refraction field n along the beam path.[6] Spatial OPD root-mean-square (OPD$_{rms}$) and OPD peak-to-peak (OPD$_{p-p}$) values are calculated to quantify the deviation from a perfectly collimated beam.

To verify the accuracy of the newly designed wavefront sensor, a benchmark experiment was conducted in the heated-jet facility at Hessert Laboratory, University of Notre Dame. A low-speed commercially available 2-D WFS[7] was used to make benchmark measurements. Streamwise realizations of rollup structures were correctly captured with both the low- and high-speed WFSs.

Section 2 of this paper presents a brief description of the Shack-Hartmann wavefront sensor's method of operation. A comprehensive discussion of the modifications of the conventional sensor, which improve the sensor's accuracy, sensitivity, and sampling rate, and a comparison with the previous generation of designed high-bandwidth WFS are presented in Sec. 3. A wavefront phase reconstruction algorithm, which was developed for the new sensor layout configuration, is presented in Sec. 4. A description of the benchmark test setup and results of the baseline flow investigation are given in Sec. 5. In addition, a comparison is made between the newly designed WFS and the commercially available sensor. The paper concludes with a discussion of the presented results and future work.

2 Shack-Hartmann Wavefront Sensors

The Shack-Hartmann wavefront sensor[6] (SHWFS) is a modification of the classical Hartmann plate test.[8] Based on the Huygens principle (which states that a ray of light travels normal to its associated optical wavefront[9]), a 2-D lenslet array with a focal length f is fixed in front of a position-sensing detector (PSD), such as a CCD or photodiodes, as shown in Fig. 1. Each lenslet subaperture is associated with a PSD, which evaluates the local 2-D transverse dot displacement ε, directly related to the local 2-D wavefront gradient θ of the wavefront phase by the equation (assuming a small θ)

$$\theta \approx \frac{\varepsilon}{f} = \nabla\Phi. \qquad (2)$$

The wavefront is reconstructed from the slopes at finitely many points, using either direct or iterative integration methods to solve Eq. (2) for the entire 2-D array.[10–12] The spatial resolution of the sensor is determined by the lenslet focal length f and subaperture spacing. The temporal reso-

lution is limited by the time required for the detector to determine the spot displacement.

3 High-Bandwidth Wavefront Sensor

Improvement in PSDs' performance and response time has enabled utilizing these detectors for fast wavefront sensing, replacing the standard CCD detectors. Ghebremichael et al.[13] presented a fast holography-based WFS, where PSDs were utilized to increase the closed-loop bandwidth. The aberrations were described via Zernike polynomials,[6] and each particular aberration converged to a unique location on the detector. The sensor demonstrated detection rates up to 1 MHz. A lateral-effect photodiode-based SHWFS was presented by Chen et al.;[14,15] the sensor was based on a 4 $\times$ 4, 84-mm-focal-length lenslet array with square subapertures, and utilized a similar number of tetralateral PSDs. Using a 12-bit analog-to-digital (A/D) converter card, the system was able to measure wavefronts at frame rates up to 5 kHz.[16]

A number of WFSs were developed by the aero-optics group at Notre Dame. The first was a 1-D small-aperture beam technique (SABT) wavefront sensor introduced by Jumper and Hugo,[17] which demonstrated a wavefront capture rate up to 100 kHz. A second generation of 8 $\times$ 8-subaperture high-bandwidth SHWFSs was designed under a joint STTR program between Notre Dame and Oceainit,[18] and wavefront capture rates up to 78 Hz were demonstrated.[7,19]

Despite the high capture rate, this WFS was associated with a number of disadvantages, mainly:

1. Tetra-lateral position-sensing detectors were used to detect the dot displacement, and these detectors exhibit a nonlinear response between the spot position and the output voltage near the detector's edges.[20]
2. The 8 $\times$ 8 subaperture layout was obtained by manually combining four 4 $\times$ 4 subaperture substrates, introducing an alignment problem.
3. A square 80 $\times$ 80-mm custom-made lenslet array with a focal length of 0.5 m was used, increasing the price of the system and the optical bench layout size.
4. Four identical voltage summation and subtraction boxes were used, increasing the electronic rack size, and BNC cables were used to connect the system components, introducing electronic noise and further adding to the complexity of the system.

The design of the new sensor was driven by addressing these disadvantages and is presented in the following subsections.

3.1 Position-Sensing Devices

As mentioned, aero-optics effects are associated with high temporal frequencies exceeding the current framing capability of commercially available WFSs based on CCD detectors; these sensors grab the spot image and then usually use a time-consuming, Gaussian-fitted data-reduction algorithm to approximate the center portion of the spot image to find the spot centroid. It should be mentioned that high-framing-rate CCD cameras do exist; however, running these cameras at high sampling frequencies reduces the pixel count available per subaperture. SHWFSs using these
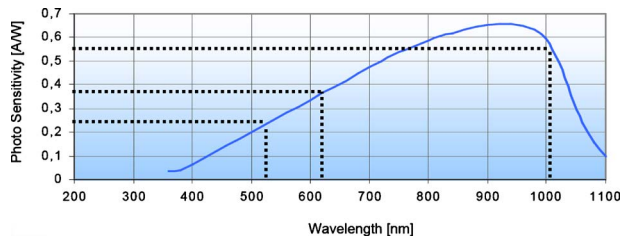
Fig. 2 Characteristic photosensitivity-versus-wavelength plot.

high-bandwidth CCD arrays have been constructed for research demonstrations;[21] however, there are still complications in turning them into real-time sensors.

The newly designed high-bandwidth WFS has 68 duo-lateral analog PSDs with an active area of 4×4-mm and a maximum rise time of 1 μs. While the tetra-lateral PSDs exhibits a position nonlinearity near the sensor edges, resulting in a larger detection error, the duo-lateral PSDs have a linear response over the entire sensor area with very small position detection error. A detailed description of the duo-lateral PSD principle of operation and characteristics can be found in Ref. 20.

The centroid of the light spots can be related to the four voltage readings from each PSD, V_i ($i = 1, \ldots, 4$), through the formulas

$$DivX = K_X \cdot \frac{V_1 - V_2}{V_1 + V_2} \qquad (3)$$

and

$$DivY = K_Y \cdot \frac{V_3 - V_4}{V_3 + V_4}, \qquad (4)$$

where K_X and K_Y are calibration coefficients, which are constant over the area of the duo-lateral detector. For each detector the voltage addition and subtraction are performed using electronic chips, while the signal divisions to obtain

$DivX$ and $DivY$ for the sensor are performed by postprocessing software.

While high frame rates and low light source intensity could cause a significant reduction in the photon counts on CCD arrays due to their digital characteristics, the problem is avoided in PSDs due to their high linearity and analog characteristics (the incident photons are directly converted into current), and the detector linearity does not depend on the light source intensity, at least theoretically. In reality, the photosensitivity of the PSDs strongly depends on the wavelength of the light source. The detectors were tested with a 2-W continuous Nd:YAG laser. Based on the manufacturer's characteristic photosensitivity-versus-wavelength plot, shown in Fig. 2, using a HeNe laser would improve the sensitivity by approximately 50%, and operating in the near infrared (IR) region, using a laser with $\lambda = 1064$-nm wavelength as an example, would improve the sensitivity by 120%.

Replacing the CCD array with an array of analog PSDs offered an accurate continuous spot position measurement and a fast response time that could not be achieved with the commercially available wavefront sensors. The time-consuming CCD data-reduction algorithm was replaced by a simple spot analog centroid measurement, achieving sampling frame rates greater than 100 kHz, and limited only by the sampling speed of the A/D conversion boards.

3.2 Detectors Layout

The 68 detectors were mounted on a single substrate and arranged in a 85-mm-diameter circular pattern (10×10 with removed corners) with 9-mm center-to-center distance between adjacent PSDs; see Fig. 3(a). The new single-board detector arrangement eliminated alignment problems that existed in the previous 8×8 WFS; see Fig. 3(b). In addition, the previous 8×8 wavefront sensor required a custom-made square lenslet array to match the lenses with the detectors, resulting in difficult alignment and, for round beams, not utilizing the corner sensors. The circular detector pattern of the new WFS is more relevant to optical tests,
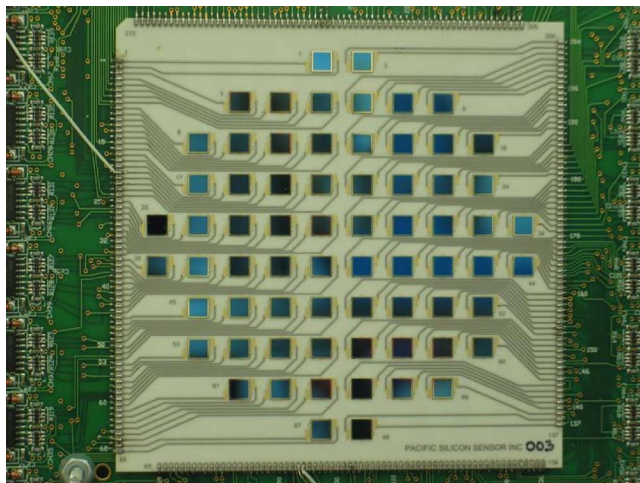
(a)
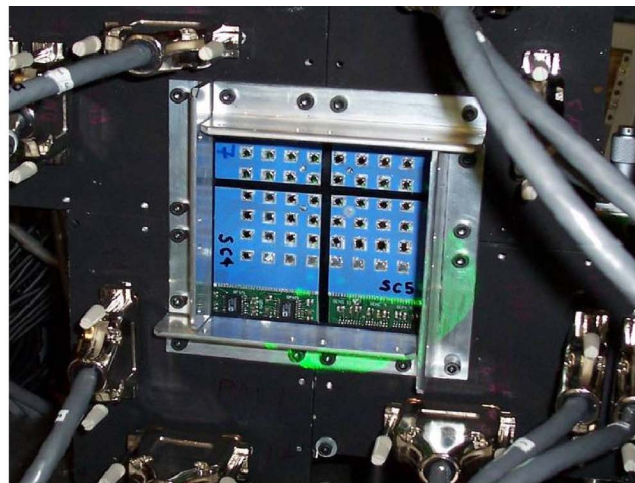
(b)

Fig. 3 Comparison between layouts of (a) the new 10×10 wavefront sensor and (b) the 8×8 wavefront sensor.
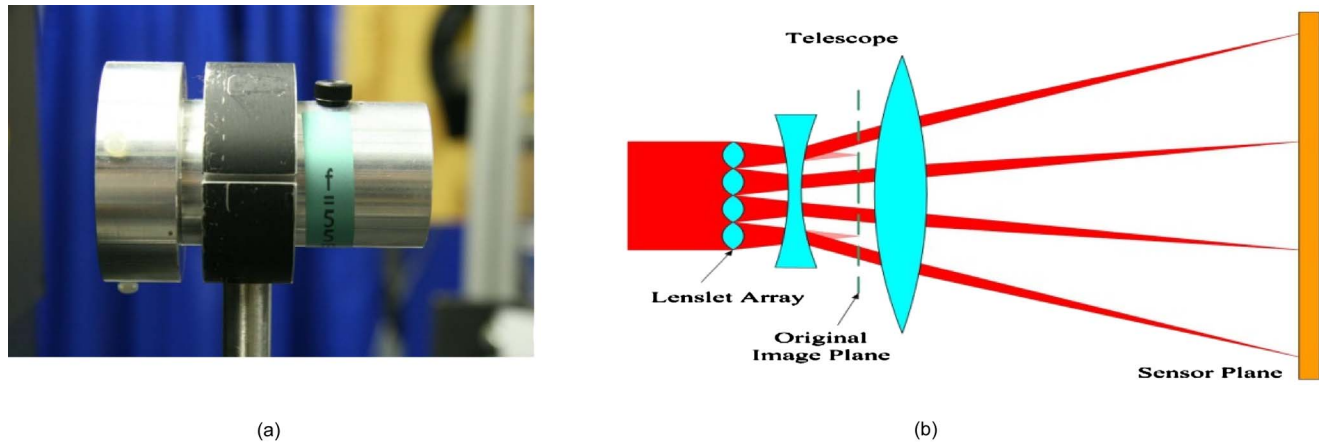
Fig. 4 (a) Designed reimaging telescope. (b) Telescope optical layout with light entering the lenslet from the left.

where a circular beam shape is usually used, and if needed, it can be directly matched with a round DM.

3.3 Electronics

The sensor electronic design was improved by designing a single multilayer board with a smaller addition and subtraction chips, and directly attached to the detector board, while the transimpedance amplifiers were mounted on the same board, decreasing the number of required connection wires, the electronic noise and the electronic-rack size significantly compared to the previous 8×8 WFS. As was mentioned, the signal divisions for the sensor are currently performed by postprocessing software, but an all-analog addition, subtraction, and division electronic board is currently being designed to provide real-time spot locations and reduce the number of sampled channels.

3.4 Lenslets, Sensor Sensitivity, and Dynamic Range

A key requirement for a wavefront sensor system is to have a small optical bench size and maximized sensitivity. A commercially available monolithic lenslet array with $p = 1$-mm pitch between lenslets, $f = 55$-mm focal length, and $D = 25$-mm diameter was chosen, reducing the lenslet array size significantly compared to the previous generation of 8×8 WFSs. To improve the sensor sensitivity and reimage the dot pattern onto the detector board, a reimaging telescope was designed to reimage the lenslet array's original image plane onto the detector plane with magnification $M = 9$ and minimal aberrations. With the telescope the lenslet focal length is increased from f to an effective focal length $f_{\mathrm{eff}} = Mf$. Figure 4(b) gives a schematic of the telescope optical layout. With the reimaging telescope the sensor sensitivity $\theta_{\min}$ can be described as

$$\theta_{\min} = \frac{\varepsilon_{\min}}{f_{\mathrm{eff}}} = \frac{\varepsilon_{\min}}{Mf}, \tag{5}$$

where $\varepsilon_{\min}$ is the minimum detectable focal spot displacement in the image plane of the WFS due to the local aberrations in the wavefront. In view of Eq. (5), aberrations that otherwise cannot be detected without the reimaging tele-

scope, due to the PSD resolution, now could be magnified and detected. Figure 4(a) presents the designed telescope case, containing the lenslet array and the reimaging lenses. Based on the detector specification, the manufacturer-provided noise-limited spot-position resolution at $\lambda = 632$ nm and 0.5 μW is 0.06 μm, which corresponds to 0.12-μrad noise-limited slope for the chosen lenslet array. It should be mentioned, however, that the noise-limited resolution value given by the manufacturer is based on testing under very controlled conditions, resulting in a very low noise level. In reality, the spot is typically limited to the minimum voltage resolution of an A/D converter; using Eqs. (3) and (4), the accuracy in measuring the spot positions for the current system was estimated as ≈ 0.15 μm/bit.

Based on Eq. (5), a comparison can be performed between the sensitivities of the two sensors. For the same input beam with diameter D, we calculate

$$\frac{\theta_{\min}^{8 \times 8}}{\theta_{\min}^{10 \times 10}} = \frac{D_{8 \times 8}}{Df_{8 \times 8}} \cdot \frac{Df_{10 \times 10}M}{D_{10 \times 10}} \approx 8, \tag{6}$$

where $D_{8 \times 8}$ and $f_{8 \times 8}$ are the 8×8 WFS lenslet array size and focal length, respectively, and $D_{10 \times 10}$ and $f_{10 \times 10}$ likewise for the new 10×10 WFS. The main reason for the sensitivity improvement is that for the new 10×10 WFS the beam is reimaged to 10-mm, resulting in increasing local slopes based on the Lagrange invariant,[9] while for the 8×8 WFS the beam had to be expanded to fit the 80×80-mm square lenslet array, thus decreasing the slopes and reducing the resolution. The dynamic range is limited by the detector's physical size, yielding the maximum dynamic range, $\theta_{\max}$, as

$$\theta_{\max} = \frac{d}{2Mf}, \tag{7}$$

where d is the detector side length (the actual active area may be limited to the central 80% of the 4×4-mm detector physical area). The trade-off between the sensor sensitivity and dynamic range was addressed by using three lenslet arrays with different focal lengths, achieving maximum re-
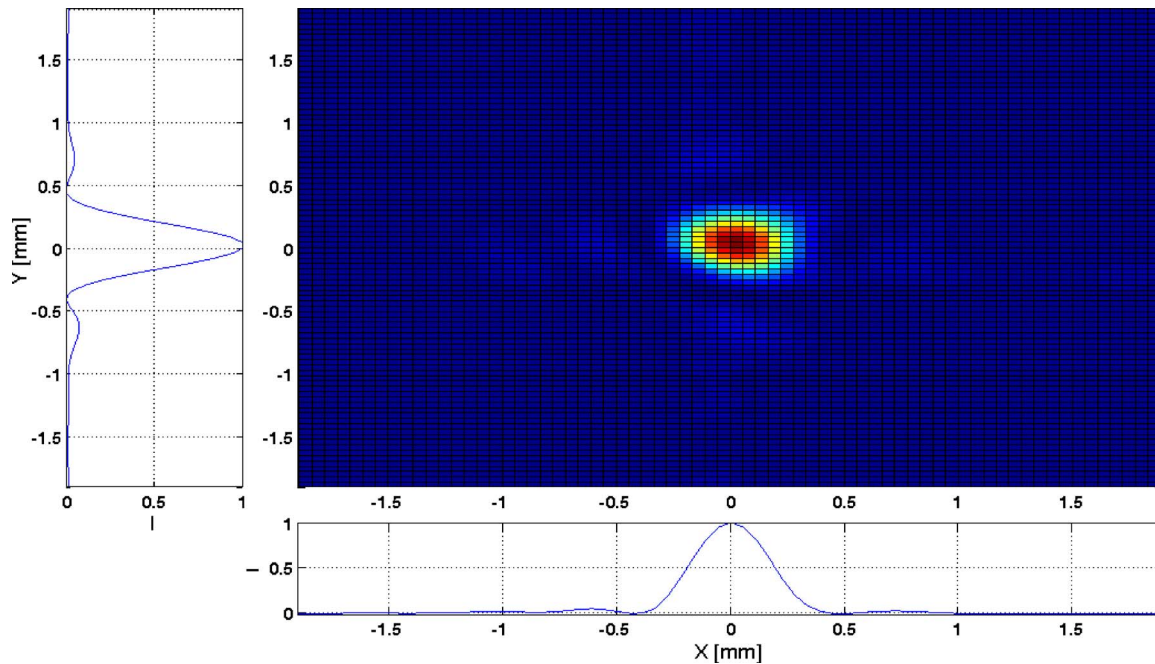
Fig. 5 Typical spot intensity pattern contour and intensity profiles in *x* and *y* directions.

solved deflection angles in the range $\theta_{max} \approx 4$ to 13 mrad.

The theoretical ratio of the largest measurable slope, θ_{max}, to the smallest detectable change in wavefront slope, θ_{min}, for the chosen lenslet array is $\approx 3 \times 10^4$. In reality, the ratio is smaller, but still large enough for most applications.

In our case, where the lenslets have a square-shaped subaperture, the diffraction-limited spot size (although the shape of the central order of a Sinc^2 pattern is not radially symmetric, the distance between the zeros along one of the axes is used here to approximate the spot size)[4] is

$$\sigma = \frac{2\lambda M f}{p}, \tag{8}$$

where *p* is the pitch between lenslet subapertures. For the chosen lenslet array, $\sigma \approx 0.5$-mm. An intensity pattern contour of a single spot and the intensity profiles in the *x* and *y* directions are shown in Fig. 5. The real spot size matched the theoretical prediction quite well.

Conventionally, another dynamic range limitation could arise due to spot overlapping causing crosstalk between two adjacent areas of interest (AOIs), as is the case with CCD detectors. In our case, this scenario is not relevant, due to the large pitch between adjacent PSDs (9 mm). Still, the light spot can leave the detector active area due to the large wavefront slope, determined by θ_{max}. That condition can be diagnosed as a drop in the detector voltage signal.

4 Wavefront Reconstruction Algorithm

An essential part of a WFS system is the wavefront reconstruction algorithm used to reconstruct the instantaneous aberrated wavefront. Different solution methods have been developed by a number of authors.[10–12] For our analysis, the Fried geometry[10] was adopted, so that each PSD was represented as a square subaperture (cell) with the mea-

sured orthogonal phase gradients in its center, and the four estimated phases (nodes) lie in the subaperture corners. Denoting the elements by (i, j), each subaperture was represented as shown in Fig. 6(a). The grid array for the 10 × 10 sensor layout is shown in Fig. 6(b). A detailed description of the wavefront reconstruction algorithm derivation can be found in Ref. 22. Here, we provide a brief description only.

A least-squares estimation was used to fit a bilinear surface to solve Eq. (2). The relation between the phase and the phase gradients, given in Eq. (2), can be written as

$$\frac{\partial \Phi}{\partial x} = \theta_x, \tag{9}$$

$$\frac{\partial \Phi}{\partial y} = \theta_y, \tag{10}$$

and

$$\frac{\partial^2 \Phi}{\partial x\, \partial y} \to 0 \tag{11}$$

when the incident wavefront is described in terms of the Cartesian coordinates (x, y). The third condition is designed to suppress high spatial frequencies that can be present in each subaperture, and to make sure that least-squares estimation has a unique solution up to an arbitrary constant. A second-order central difference method can be used to discretize the partial derivative, and Eqs. (9)–(11) can be rewritten using matrix notation. For the 10 × 10 wavefront sensor, the matrix dimensions are 68 × 89. To find a unique solution, a zero wavefront value should be imposed on one of the nodes, $\Phi(x_0, y_0) = 0$, or one may require that
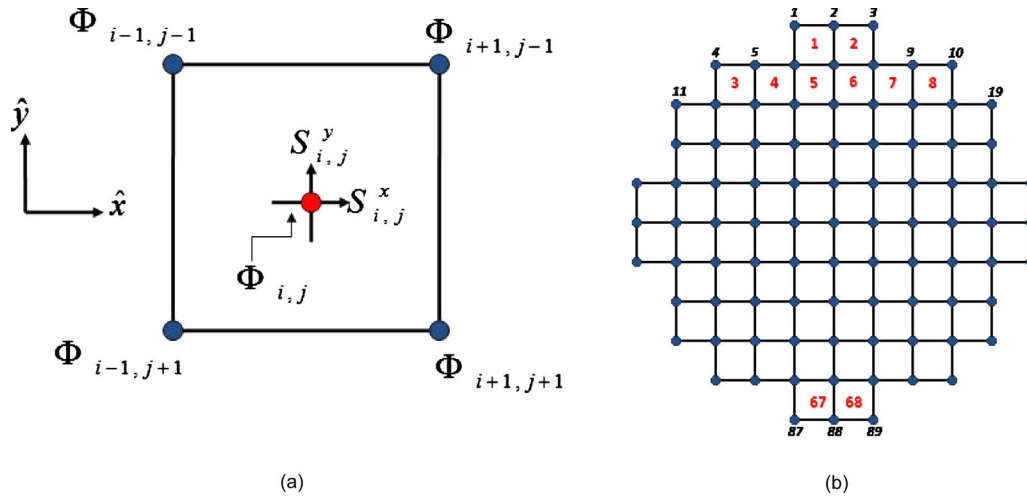
(a)

(b)

Fig. 6 (a) Fried[10] cell geometry. The measured phase gradients are at the center, and the estimated phases lie at the corners (nodes). (b) Wavefront sensor grid array with 68 cells and 89 nodes.
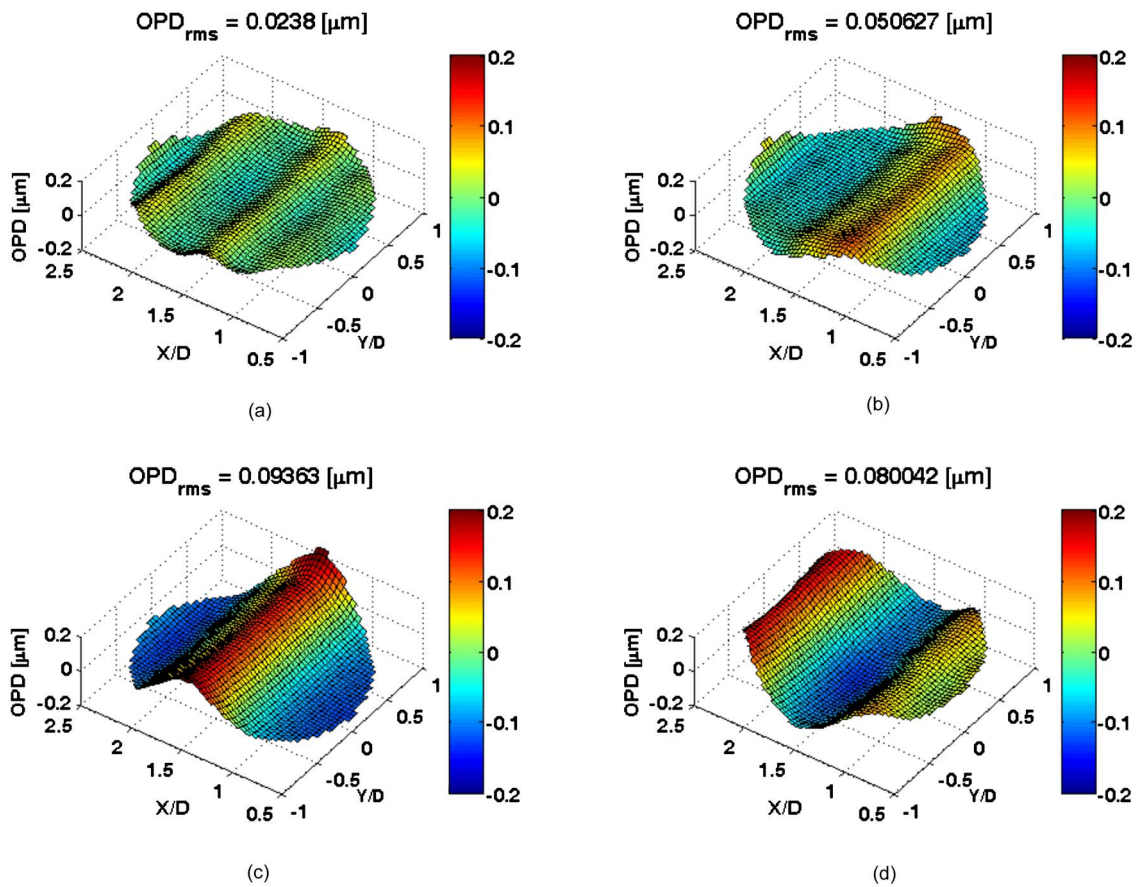

(a)

(b)

(c)

(d)

Fig. 7 Typical instantaneous wavefronts realizations (2-D view) obtained with the high-bandwidth wavefront sensor for a wave propagating in the streamwise (x) direction ($1/2 < X/D < 5/2$; $-1 < Y/D < 1$).
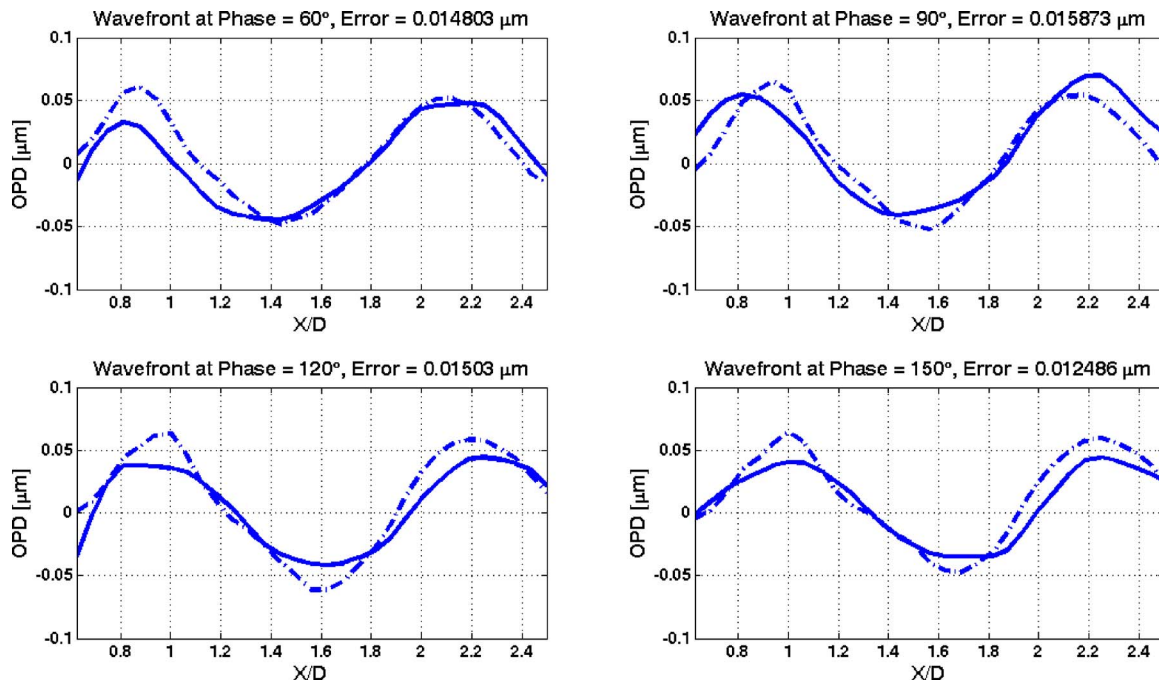
Fig. 8 Comparison of phase-locked averaged wavefront measurements: high-bandwidth sensor (solid line), CLAS-2D sensor (dashed line) $(0.625 < X/D < 2.5)$.

$\int_{Ap} \Phi(x,y) \, dx \, dy = 0$. The least-squares estimation can be finally written as

$$\Phi = C_x \theta_x + C_y \theta_y, \qquad (12)$$

where the reconstruction matrices, C_x and C_y, are independent of the input measured slopes, and need only be calculated once for a given sensor layout configuration and then stored. If needed, the reconstruction matrices can be stored directly on a digital multiplication board integrated in a real-time AO system, thereby reconstructing the wavefront efficiently and with minimum system latency.

5 Two-Dimensional Heated-Jet Validation Experiments

Experiments were conducted at the heated-jet facility at the University of Notre Dame to verify the accuracy of the newly designed WFS. A detailed description of the facility the jet's response to a 240-Hz forcing, and flow measurements can be found in Refs. 23–26. In addition, a detailed description and schematic of the optical train, electronics setup, and sensor calibration and data processing can be found in Ref. 27.

5.1 Forced-Flow Results

Although the 10×10 sensor is able to sample wavefronts at a rate of 104 kHz, for this test time-resolved raw voltage signals were sampled at the lower rate of 24 kHz. The time-resolved wavefronts give further insight into the periodic and growing nature of the aberrating flow field; the convective nature of the regularized aberration in the streamwise direction x is well demonstrated by the structure propagating through the beam aperture, and the presumption that the jet is essentially two-dimensional, due to the acoustically

forcing, is validated by noticing that the wavefront profile in the x direction is the same in all spanwise directions y. Four typical instantaneous two-dimensional wavefront realizations are presented in Fig. 7. An initial aberration structure rollup is shown to start developing around $X/D=1$ [Fig. 7(b)], reach a maximum aberration amplitude of approximately 0.2 μm around $X/D=2$ [Fig. 7(c)], and start breaking down thereafter [Fig. 7(d)]. The mean OPD_{rms} and OPD_{p-p} values were 0.059 and 0.25 μm, respectively.

5.2 Comparison of Wavefront Sensors

In order to both validate and test the spatial resolution of the high-bandwidth WFS, wavefronts from the 10×10 sensor were compared with those from another sensor. The 10×10 sensor was synchronized with a commercially available Wavefront Sciences CLAS-2D WFS,[7] which, although having a slower capture rate, has a higher spatial resolution of 33×44 subapertures. Both sensors were triggered to sample at 20 Hz.

Due to the periodicity of the acoustically forced heated jet, a phase-locked averaging was preformed to compare results from the two sensors. The averaging, over 400 cycles, was performed for 12 phase angles with a separation between angles of 30 deg. A one-dimensional slice at the center of the two-dimensional wavefronts was used to simplify the comparison. A comparison between the two sensors for the selected phase angles is presented in Fig. 8. The beam's aperture was clipped by 1.6-mm at the upstream edge to remove errors due to a drop in beam intensity at that edge $(0.625 < X/D < 2.5)$.

The comparison between the two WFSs reveals that, although the high-bandwidth WFS has only a modest spatial resolution of 10×10 subapertures, it captured and reconstructed all the essential features of the two-dimensional

convecting aberration. Further, despite the small peak-to-peak aberration amplitude (an average of OPD_{p-p} =0.11 μm for both sensors), the high-bandwidth sensor was able to resolve the peak-to-peak aberration amplitude correctly as compared with the higher-spatial-resolution CLAS-2D WFS.

Wavefront slices from the high-bandwidth 10×10 WFS were fitted with a cubic polynomial to compare them with the wavefront slices acquired by the CLAS-2D WFS. For each phase angle a spatial matching error was calculated based on the equation

$$\text{error} = \left[\frac{\Sigma_{i=0}^{N}[OPD_{10\times10}^{i} - OPD_{CLAS-2D}^{i}]^2}{N} \right]^{1/2}, \quad (13)$$

where N is the number of spatial points in the streamwise direction x. The calculated error for each phase is presented in Fig. 8. A mean error of 0.0176 μm was calculated for these 12 phase angles; this value is within 20% of the mean OPD_{p-p} of both WFSs.

6 Conclusion

An analog high-bandwidth two-dimensional WFS was developed and tested against a commercially available CLAS-2D Wavefront Sciences WFS. The analog nature of the new sensor enables a high sampling rate for aero-optical convecting aberrations, capable of capture rates greater than 100 kHz, which is essential for investigating aero-optical effects and developing adaptive optics systems that can mitigate high-content temporal bandwidth frequencies. It was shown that despite the modest spatial resolution, the new sensor was capable of resolving the essential spatial character of aberrating structures.

The high-bandwidth WFS can be used in two major ways. The first is as part of a conventional real-time (or pseudo-real-time) adaptive optics system to diagnose and compensate for optical disturbances at high temporal rates, while maintaining the system stability. Secondly, the WFS can be used as a diagnostic tool, investigating optical disturbances associated with turbulent flows, which could not be addressed before, due to the limited sampling rate capability of the currently available state-of-the-art WFSs. Currently, the high-bandwidth WFS has a maximum frequency of 104 kHz; this limit is due to the bandwidth limitation of presently used data acquisition system and can be improved with a faster data acquisition system.

References

1. E. J. Jumper and E. J. Fitzgerald, "Recent advances in aero-optics," *Prog. Aerosp. Sci.* **37**(3), 299–339 (2001).
2. J. Siegenthaler, E. J. Jumper, and S. Gordeyev, "Propagation vs. aero-optics," AIAA Paper 2008-1076 (2008).
3. A. Nightingale, S. Gordeyev, E. J. Jumper, B. Goodwine, and J. Siegenthaler, "Regularizing shear layer for adaptive optics control applications," AIAA Paper 2005-4774 (2005).
4. J. Goodman, *Introduction to Fourier optics*, McGraw-Hill, New York (1996).
5. J. H. Gladstone and T. P. Dale, "Researches on the refraction, dispersion, and sensitiveness of liquids," *Philos. Trans. R. Soc. London* **153**, 317–343 (1863).
6. R. K. Tyson, *Principles of Adaptive Optics*, Academic Press, Boston (1991).
7. D. Cavalieri, D. Wittich, S. Gordeyev, K. Cheung, and E. J. Jumper, "Aero-optical measurements using high-bandwidth two-dimensional wavefront sensor array," *J. Directed Energy* **2**(4), 285–296 (2007).
8. D. Malacara, *Optical Shop Testing*, Wiley, New York (1978).
9. M. Klein, *Optics*, Wiley, New York (1970).
10. D. L. Fried, "Least-square fitting a wavefront distortion estimate to an array of phase-difference measurements," *J. Opt. Soc. Am.* **67**(3), 370–375 (1977).
11. R. H. Hudgin, "Wavefront reconstruction for compensated imaging," *J. Opt. Soc. Am.* **67**(3), 375–378 (1977).
12. W. H. Southwell, "Wave-front estimation from wave-front slope measurements," *J. Opt. Soc. Am.* **70**(8), 998–1006 (1980).
13. F. Ghebremichael, G. P. Andersen, and K. S. Gurley, "Holography-based wavefront sensing," *Appl. Opt.* **47**(4), A62–A69 (2008).
14. K. Chen, Z. Yang, H. Wang, E. Li, F. Yang, and Y. Zhang, "PSD-based Shack-Hartmann wavefront sensor," in *Adaptive Optics and Applications III*, *Proc. SPIE* **5639**, 87–94 (2004).
15. K. Chen, Z. Yang, E. Li, H. Wang, F. Yang, and Y. Zhang, "Performance of the PSD-based Hartmann-Shack wavefront sensor," in *5th Int. Workshop on Adaptive Optics for Industry and Medicine*, *Proc. SPIE* **6018**, 261–270 (2005).
16. J. Lin, J. Tang, and H. Chen, "High-speed wavefront sensor based on position sensitive detectors (PSDs)," in *Adaptive Optics and Applications III*, *Proc. SPIE* **5639**, 95–102 (2004).
17. E. J. Jumper and R. J. Hugo, "Quantification of aero-optical phase distortion using the small-aperture beam technique," *AIAA J.* **33**(11), 2151–2157 (1995).
18. Air Force Office of Scientific Research (AFOSR), under grant No. F49620-02-C-0031.
19. S. Gordeyev, D. Duffin, and E. J. Jumper, "Aero-optical measurements using Malley probe and high-bandwidth 2-D wavefront sensor," presented at Int. Conf. on Advanced Optical Diagnostics in Fluids, Solids and Combustion, Tokyo (2004).
20. J. Graeme, *Photodiode Amplifiers: Op Amp Solutions*, McGraw Hill, Boston (1966).
21. C. M. Wyckham, S. H. Zaidi, R. B. Miles, and A. J. Smits, "Measurement of aero-optic distortion in transonic and hypersonic, turbulent boundary layers with gas injection," AIAA Paper 2005-4755, presented at 36th AIAA Plasmadynamics and Lasers Conf., Toronto (2005).
22. S. Abado, S. Gordeyev, and E. J. Jumper, "Designing and testing a high-bandwidth 2-D wavefront sensor for aero-optics," in *Advanced Wavefront Control: Methods, Devices, and Applications VII*, *Proc. SPIE* **7466**, 746602 (2009).
23. R. J. Hugo, "Quantifying the spatio-temporal effects of optically-active turbulent flow fields on a coherent optical wave," PhD Dissertation, Dept. of Aerospace and Mechanical Engineering, Univ. of Notre Dame, Notre Dame, IN (1995).
24. R. J. Hugo and E. J. Jumper, "Implications of the homogeneous turbulence assumption on the aero-optic linking equation," *Opt. Tech. Fluid Thermal and Combustion Flow, SPIE Proc.* **2549**, 189–200 (1995).
25. R. J. Hugo and E. J. Jumper, "Experimental measurement of a time-varying optical path difference by the small-aperture beam technique," *Appl. Opt.* **35**(22), 4436–4447 (1996).
26. R. J. Hugo and E. J. Jumper, "Constant current anemometry and its impact on aero-optical measurements," AIAA Paper 1995-1986, presented at 26th Plasmadynamics and Lasers Conf. (1996).
27. S. Abado, S. Gordeyev, and E. J. Jumper, "Designing and testing a new Shack-Hartmann high bandwidth two-dimensional wave front sensor," AIAA Paper 2009-4225, presented at 40th AIAA Plasmadynamics and Lasers Conf., San Antonio, TX (2009).

Shaddy Abado received his BSc degree in mechanical engineering at the Technion–Israel Institute of Technology, Haifa, Israel, in 2005. He is currently pursuing his PhD degree in aerospace engineering at the University of Notre Dame. He is currently working on a two-dimensional wavefront sensor for aero-optics.

Stanislav Gordeyev received his MS in applied physics in 1991 from the Moscow Institute of Physics and Technology, Moscow, Russia, and his PhD in aerospace science in 1999 from the University of Notre Dame. Currently he is an assistant research professor in the Department of Aerospace and Mechanical Engineering, University of Notre Dame. His research interests include fundamental and applied aspects of aero-optical problems and low-dimensional modeling of complex systems.

Eric J. Jumper is a professor in the Department of Aerospace and Mechanical Engineering at the University of Notre Dame.